THE UNIVERSITY *of* EDINBURGH

Edinburgh Research Explorer

Molecular design of nanohybrid gas separation membranes for optimal CO2 separation
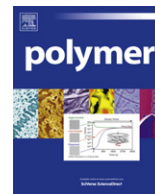
Molecular design of nanohybrid gas separation membranes for optimal CO$_2$ separation

Cher Hon Lau [a], Donald R. Paul [a,b], Tai Shung Chung [a,*]

[a] Department of Chemical & Biomolecular Engineering, National University of Singapore, 4 Engineering Drive 4, 117576 Singapore, Singapore
[b] Department of Chemical Engineering, The University of Texas at Austin, Austin, TX 7812 0231, USA

ARTICLE INFO

ABSTRACT

Organic-inorganic materials comprising CO$_2$-philic components may yield superior CO$_2$ transport properties and good CO$_2$/H$_2$ gas selectivity. We report that a fine balance in size heterogeneity in the silicon-based structures is essential and a mixture of sizes up to 50 nm surrounded by 5–15 nm silicon-based nanostructures is the preferred inorganic phase morphology that yields optimal nanohybrid membranes. The combination of optimal synthesis conditions i.e. water/silicon ratio, condensation and ozone pre-treatment durations yields a nanohybrid membrane with a CO$_2$ permeability of 2000 Barrer while achieving a CO$_2$/H$_2$ selectivity of 11. The findings of this work are important for the design of gas separation membranes using green materials.

1. Introduction

The capture of the greenhouse gas carbon dioxide (CO$_2$) from flue gas streams (N$_2$) has become a major industrial concern in recent years [1]. CO$_2$ also exists as a byproduct in syngas (H$_2$) production [2] and is an impurity in some natural gas (CH$_4$) sources [3]. In all these cases, CO$_2$ must be separated from these gas streams. Traditional gas separation technologies are costly, energy intensive, and often are not environmental friendly. A "green" alternative to traditional gas separation processes is polymeric membrane technology. Gas separation membranes are cost-effective with low carbon footprints [4]. The operating principles of polymeric gas separation membranes are summarized by the following two equations: $P = S \times D$ and $\alpha = P_A/P_B$ where P is the gas permeability of the membrane, S and D refer to the solubility and diffusivity coefficients of a gas penetrant in the polymer matrix, while α is the selectivity of the permeation of gas A relative to gas penetrant B and defines the degree of separation that can be achieved by the membrane material. The properties P and α are the key performance indices of a membrane material for gas separation.

Membrane materials may exist in the form of simple polymers [5–7] to molecularly designed polymers [8–10] and nano-composites [11–13]. Nanocomposites, also commonly known as mixed matrix membranes, is a form of material hybridization that harnesses the advantages of polymers and inorganic nano-structures [14–17]. These hybrid materials are potential candidates for membrane fabrication. Such inorganic nanostructures have been used to enhance gas transport properties [18], reduce polymer crystallinity [19], and augment mechanical properties [20] of mixed matrix membranes. However, the gas separation performance of mixed matrix membranes is highly dependent on the size and uniform dispersion of the inorganic nanostructures in the polymer matrix. Compatibility with the polymer and Ostwald ripening effects can impede the uniform dispersion of nanostructures [21]; however, in situ synthesis of nanostructures in the polymer matrix, e.g., by a sol-derived organic-inorganic material [22–24], provides a route for dealing with such issues.

At near ambient operating conditions, organic-inorganic materials derived from polyethylene oxide (PEO), polypropylene oxide (PPO) and silicon-based nanostructures comprise high CO$_2$ affinity components and possess high CO$_2$ permeability with good CO$_2$/H$_2$ separation capabilities [20,22,23,25] that are comparable to pure polymeric rubbery membranes [26]. In these organic-inorganic membranes, the polyether matrix influences the Si–O–Si network connectivity, while building up an alternative polyether network via polymerization or polycondensation that enhances CO$_2$/light gas selectivity. Additionally, the polar ether oxygens in PEO interact favorably with acidic CO$_2$ penetrants via a dipole–quadrapole interaction [27], while the pendant methyl group in PPO enhances CO$_2$ permeability by increasing the relative fractional free volume

* Corresponding author. Tel.: +65 6874 6645; fax: +65 6779 1936.
E-mail address: chencts@nus.edu.sg (T.S. Chung).

[28]. Such organic-inorganic materials are synthesized via an acid-catalyzed sol-gel process that involves the hydrolysis of $Si-OCH_3$ moieties to Si-OH bonds, followed by condensation of the Si-OH bonds to form irreversible $Si-O-Si$ cross-links [29,30]. The $Si-O-Si$ networks increase the mechanical stability of these organic-inorganic materials [20] and impart higher CO_2 affinity to the organic-inorganic materials [25]. The grafting of short alkyl chains onto the main chains of these organic-inorganic materials yield nanohybrid materials with CO_2 permeability comparable to the CO_2 permeability of PDMS (same order of magnitude), while obtaining a CO_2/H_2 selectivity value that is ~ 5 times larger than that of PDMS [25]. The distribution of the silicon-based nanostructures is the key to ultrahigh CO_2 permeability and high CO_2/H_2 selectivity. To determine the actual mechanisms behind the significant improvements in membrane properties, the morphology of the inorganic phase in this nanohybrid material must be more extensively characterized. This work addresses the relationship between the inorganic phase morphology and the CO_2 permeability and CO_2/H_2 separation of these nanohybrid materials. The inorganic phase morphology can be controlled via sol-gel reaction kinetics that is influenced by organic-inorganic ratio, water/silicon ratio [30], synthesis conditions, and the degree of material modification.

2. Materials and experimental details

2.1. Materials

Jeffamine® ED-2003 ($M_w = 2000$ g/mole) was used in this work; it is a commercially available water soluble polyther diamine derived from a propylene oxide end-capped polyethylene glycol i.e., the polyether segment structure is polypropylene oxide − polyethylene oxide − polypropylene oxide (PPO-PEO-PPO). Polyethylene glycol methacrylate (PEGMA: $M_w = 360$ g/mole), ethanol (HPLC grade) and 3-glycidyloxypropyltrimethoxysilane (GOTMS: $M_w = 236$ g/mole) were purchased from Sigma Aldrich, Singapore. Hydrochloric acid (HCl) was purchased from Fisher Scientific. All chemicals and solvents, except for PEGMA, were used as received. The inhibitors in PEGMA were removed using activated carbon. For every 100 mL of PEGMA, 4 g of activated carbon was added and stirred for 1 h, after which, the activated carbon was filtered from this mixture. These procedures were repeated 3 times. The purified PEGMA was stored at 4 °C.

2.2. Synthesis and modification of organic-inorganic materials

In the first part of this work, the effects of the organic/inorganic wt.% ratio on gas permeation was studied by varying the organic/inorganic content from 50/50 wt.% to 75/25 wt.% to 80/20 wt.%. GOTMS was first hydrolysed for 30 min at room temperature using a catalyzing aqueous solution containing 37.5 wt.% HCl. Subsequently, the hydrolysed alkoxysilane solution was added to a solution consisting of PPO-PEO-PPO diamine dissolved in 70 wt.% ethanol and 30 wt.% deionized water. The epoxy−amine reaction and preliminary condensation occurred during magnetic stirring at 750 rpm at 70 °C for 1 h. These organic-inorganic materials are coded $PED_{xx}S_{yy}$, whereby PED represents the polyether diamine while S represents the alkoxysilane; the subscripts denotes the amount of component in wt.%.

In the second part, the effects of condensation time on gas permeation in organic-inorganic materials were studied for $PED_{xx}S_{yy}$ materials with the largest CO_2 permeability value i.e. $PED_{80}S_{20}$ materials. $PED_{80}S_{20}$ solutions were synthesized using the aforementioned protocol for different condensation durations, ranging from 1 to 24 h. These materials are coded $PED_{80}S_{20}$-xh, whereby "xh" denotes the condensation time in hours.

In the third part, the effects of ozone pre-treatment time on gas permeation were studied for organic-inorganic materials with optimal CO_2/H_2 selectivity i.e. $PED_{80}S_{20}$-1 h materials. $PED_{80}S_{20}$-1 h solutions were first synthesized and allowed to cool to room temperature prior to 30, 60, 180 and 300 s of ozone pre-treatment. Ozone pre-treatment was carried out using an AC Faradayozone − high concentration ozone generator (L10 G). High purity oxygen contained in a 10 L bottle was obtained from SOXAL, Singapore and was converted into ozone (ozone flow was limited to 0.5 L per minute). Upon ozone pre-treatment, 43 wt.% of PEGMA were added to the ozone pre-treated mixture and the resultant solution was stirred at 70 °C for 24 h to facilitate PEGMA grafting onto the PEDS main chains. The ozone-modified $PED_{80}S_{20}$-1 h materials are coded $PED_{80}S_{20}$-oXs, whereby "o" represents ozone-modified materials and "Xs" stands for the pre-treatment duration in seconds.

In the fourth part, the effects of side chain concentration on gas permeation properties were investigated for ozone-modified materials with the largest CO_2 permeability value. $PED_{80}S_{20}$ were first synthesized with 1 h of condensation and pre-treated with ozone for 60 s. Subsequently, a pre-determined amount of PEGMA was added to the aforementioned solution. PEGMA grafting was facilitated via magnetic stirring at 70 °C for 24 h. Depending on the PEGMA graft concentration, the nanohybrid materials are coded $PED_{80}S_{20}$-Pxx, whereby "xx" stands for the wt. % of PEGMA graft content.

2.3. Membrane fabrication

Using a slow casting method in a Teflon dish, the organic-inorganic membranes were fabricated via an initial solvent evaporation process at 30 °C for 24 h and a subsequent evaporation process at 40 °C in a temperature controlled environment. Residual solvent was removed by drying the nascent films in a vacuum at 70 °C for 24 h. To remove unreacted monomers, all membranes were immersed in deionized water for 5 days and dried. The deionized water was changed everyday. These nanohybrid membranes were stored in a dry box at 27% humidity and 25 °C prior to testing and characterization.

2.4. Membrane characterization

A Perkin Elmer Fourier Transform Infrared (FTIR) Spectrometer (Spectrum 2000) was used to characterize the chemical structures of the working materials. Prior to measurements, the spectrometer was purged with nitrogen gas for 30 min. After placing a sample into the FTIR spectrometer, the system was purged with nitrogen gas for another 30 min. FTIR measurements in the attenuated total reflectance (ATR) mode were performed over 64 scans in the range of 600–4000 cm^{-1}. The resolutions of the spectra were 4 cm^{-1}. The data were analyzed using Spectrum Version 5.3 (analytical software).

The presence of $Si-O-Si$ networks in the working membrane materials were validated using solid-state ^{29}Si. The ^{29}Si (79.5 MHz) solid-state NMR with magic angle spinning (MAS) at 7.5 kHz was performed using a Bruker DRX 400 spectrometer. Prior to solid-state NMR analysis, the organic-inorganic materials were ground via freeze milling.

To determine the crystallinity, glass transition (T_g) and melting (T_m) temperatures of the organic-inorganic membranes, differential scanning calorimetry (DSC) was performed using a DSC822^e (Mettler Toledo) calorimeter. The temperature range was from −100 °C to 100 °C with a heating rate of 10 °C/minute in a N_2 environment. The second heating curve was used for analysis in this work.

High-angle annular dark field scanning-transmission electron microscopy (HAADF-STEM) was used to observe inorganic phase morphology and dispersion. To prepare samples for HAADF-STEM
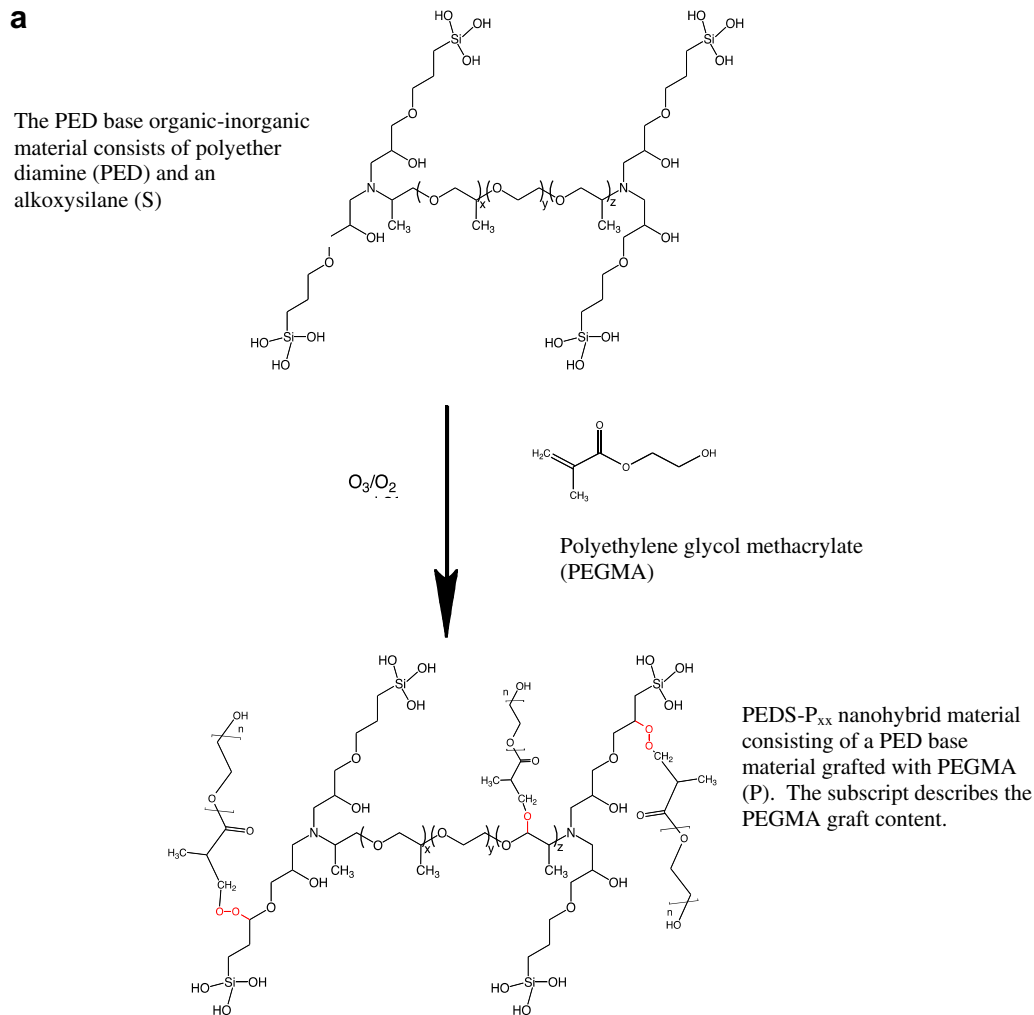
a

The PED base organic-inorganic material consists of polyether diamine (PED) and an alkoxysilane (S)

O_3/O_2

Polyethylene glycol methacrylate (PEGMA)

PEDS-P_{xx} nanohybrid material consisting of a PED base material grafted with PEGMA (P). The subscript describes the PEGMA graft content.

Fig. 1. (a): The organic-inorganic base material is pre-treated with ozone prior to condensation. The pre-ozone treatment step introduces peroxide moieties that act as radical sites for PEGMA grafting onto the organic-inorganic main chains to yield a nanohybrid membrane. (b): ATR-FTIR spectra of PED$_{80}$S$_{20}$ materials that were synthesized using 3 h of condensation (PED$_{80}$S$_{20}$-3 h), and PED$_{80}$S$_{20}$ materials that were synthesized using 1 h of condensation and different ozone pre-treatment durations ranging from 30 to 300 s (PED$_{80}$S$_{20}$-oXs with "o" indicating that these PED$_{80}$S$_{20}$ materials were modified with ozone pre-treatment while "X" denotes the ozone pre-treatment duration). (c): Solid-state ^{29}Si NMR of (i) PED$_{80}$S$_{20}$-3h, (ii) PED$_{80}$S$_{20}$-24h, (iii) PED$_{80}$S$_{20}$-o30s, and (iv) PED$_{80}$S$_{20}$-o300s organic-inorganic membranes. T^2 peaks represent partially condensed Si atoms that consist of 2 siloxane bonds and a methoxy or an ethoxy bond; while T^3 peaks represent fully condensed Si atoms with 3 siloxane bonds.

characterization, solutions containing the organic-inorganic materials were diluted from 2 wt.% to ~ 0.01 wt.%. The diluted solution was pipetted onto a 200 mesh copper Formvar/carbon TEM grid that was purchased from Electron Microscopy Sciences. A thin film of the organic-inorganic material was formed on the TEM grid upon solvent evaporation in ambient conditions. HAADF-STEM studies and EDX analysis were carried out using a FEI Titan 80-300 electron microscope equipped with an electron beam monochromator, an energy dispersive X-ray spectrometer (EDX) and a Gatan electron energy loss spectrometer. The accelerating voltage of the electron beam was 200 KeV. The scanning electron beam size of EDX measurement was around 0.3 nm. As the HAADF operation principle relies on atomic number (Z)- contrast imaging, HAADF images show little or no diffraction effects while the brightness intensity of these images is approximately proportional to Z^2 [31]. Hence, the bright shapes in STEM tomographs comprise of elements with a large Z number i.e. inorganic elements in contrast to those in the polymer matrix. Additionally, the intensity of these bright shapes can be attributed to the concentration of inorganic elements.

2.5. Gas permeation and sorption measurements

The pure gas permeabilities were determined using a constant volume and variable pressure method used in previous studies [25,32,33]. H$_2$ and CO$_2$ permeabilities at 3.5 atm were determined from the rate of downstream pressure build-up rate (dp/dt) obtained when permeation reached a steady state according to Equation (1):

$$P = D \times S = \frac{273 \times 10^{10}}{760} \frac{VL}{AT\left[\frac{p_2 \times 76}{14.7}\right]} \left(\frac{\mathrm{d}p}{\mathrm{d}t}\right) \qquad (1)$$

P refers to the permeability of a membrane to a gas and its unit is in Barrer (1 Barrer = 1×10^{-10} cm^3 (STP)-cm/cm^2 sec cm Hg) [34], D is the average effective diffusivity (cm^2/s), S is the apparent sorption coefficient/solubility (cm^3 (STP)/cm^3 polymer cm Hg), V is the volume of the downstream chamber (cm^3), L is the film thickness (cm). A refers to the effective area of the membrane (cm^2), T is the experimental temperature (K) and the pressure of the feed gas in the upstream chamber is given by p_2 (psia).
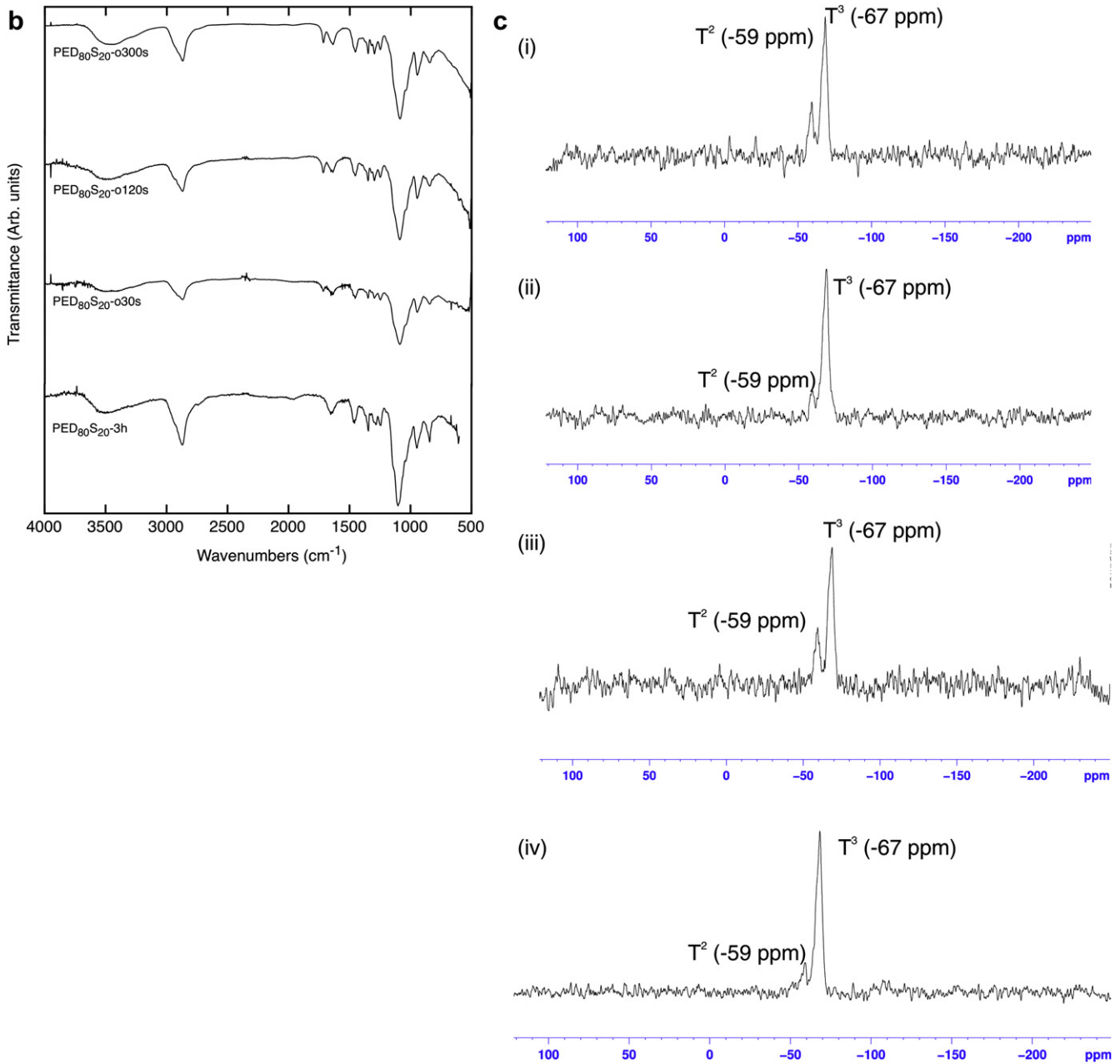
b

c

Fig. 1. (*continued*).

A mixed gas mixture containing x-mol. % of H_2 in CO_2 was used as the feed gas mixtures and the measurements were conducted at 35 °C with a CO_2 partial pressure of 3.5 atm. The molar concentrations of H_2 tested in this work are 50 mol%. To ensure constant gas molarity in the retentate, small amounts of retentate are slowly discharged into water or the atmosphere via a silicon piping. The sampling process was initiated by evacuating the line from the receiving volume (the lower chamber: downstream) to GC by vacuum pump. The compositions of the feed and permeate were analyzed by GC. The choice of carrier gas in the GC setup is nitrogen. Similar to the pure gas permeability, the mixed gas steady state permeation rate were then determined by following equations:

$$P_{H_2} = \frac{273 \times 10^{10}}{760} \frac{(1 - y_{CO_2})VL}{AT(76/14.7)[(1 - X_{CO_2})p_2]} \times \left(\frac{dp_1}{dt}\right) \quad (2)$$

$$P_{CO_2} = \frac{273 \times 10^{10}}{760} \frac{y_{CO_2}VL}{AT(76/14.7)[(X_{CO_2})p_2]} \times \left(\frac{dp_1}{dt}\right) \quad (3)$$

where P_{CO_2} and P_{H_2} are, respectively, the gas permeability of CO_2 and H_2 (Barrer), p_2 is the upstream feed gas pressure (psia), p_1 is the downstream permeate gas pressure (psia), x_{CO_2} is the mole fraction of CO_2 in the feed gas (%) and y_{CO_2} is the mole fraction of CO_2 in the permeate (%), V is the volume of the downstream chamber (cm^3), L is the film thickness (cm).

Carbon dioxide sorption tests were conducted using a Cahn D200 microbalance sorption cell at 35 °C over a pressure range of 0–250 psi (0–17.24 bar). For each sample, films with thickness of 300 μm, sides of 1 cm, and total mass of approximately 80–100 mg were placed on the sample pan. The system was evacuated for 24 h prior to testing. The gas at a specific pressure was fed into the
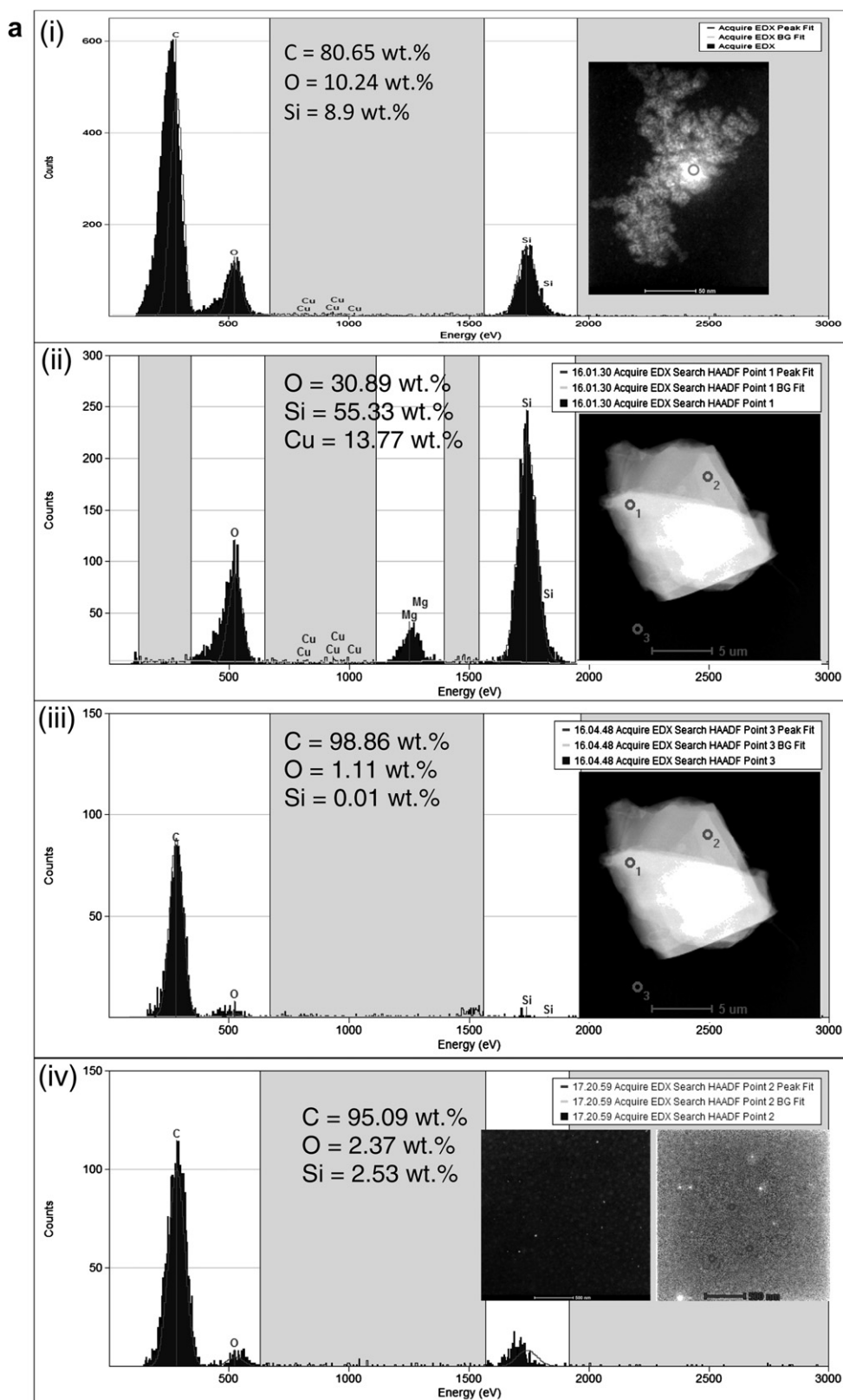
Fig. 2. (a): EDX analysis of (i) PED$_{80}$S$_{20}$-1 h, (ii) inorganic phase of the PED$_{80}$S$_{20}$-24 h material, (iii) organic phase of the PEDS-24 h material, (iv) PED$_{80}$S$_{20}$-o300 s. (b): HAADF-STEM images of organic-inorganic materials with different amounts of polyether diamine and alkoxysilane. These organic-inorganic materials were synthesized with 1 h of condensation and were not modified by ozone pre-treatments. According to the operating principle of HAADF-STEM, bright spots correspond to elements with high Z number, e.g., Si in these organic-inorganic materials. Hence, these bright spots are silicon-based nanostructures. The sizes of the silicon-based nanostructures grow as a function of increasing polyether content. (c): Pure gas permeability of PEDS with different polyether content synthesized with 1 h of condensation and no ozone modification. By adjusting the polyether content i.e. the organic/inorganic ratio during synthesis, the polyether content was varied from 50 wt.% to 80 wt.%. (d): S_{CO_2} (solid line) and D_{CO_2} (dotted line) coefficients of organic-inorganic materials with different polyether content. The lines provide a guide to the eye. All gas permeation tests were made at 35 °C and 3.5 atm. Uncertainty in permeability measurements is ±10%. The sizes of the silicon-based nanostructures in these organic-inorganic materials are also shown. 1 Barrer = 1 × 10^{-10} cm^3 (STP)-cm/cm^2 sec cm Hg.
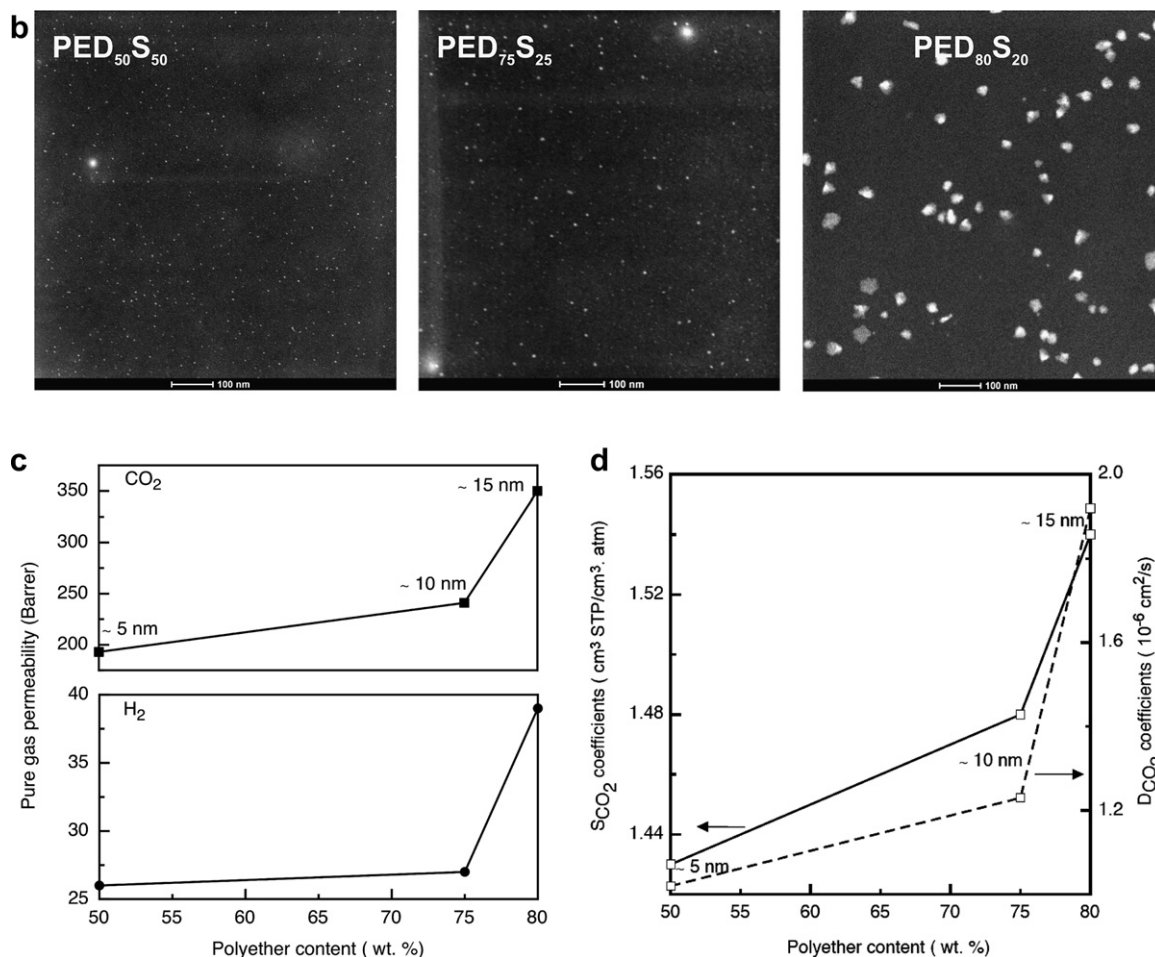
Fig. 2. (continued).

system. The mass of gas sorbed by the membranes at equilibrium was recorded. Subsequent sorption experiments were done by further increment of the gas pressure. The equilibrium sorption values obtained were corrected for buoyancy effects. CO_2 solubility coefficients of each sample were obtained from the slope of the sorption isotherms. Subsequently, CO_2 diffusivity coefficients were calculated using $D = P/S$.

3. Results and discussions

3.1. Chemical structure of working materials

Fig. 1(a) shows the chemical structure of a base material fabricated via an epoxy–diamine reaction in aqueous solutions and the modification of this base material using ozone pre-treatments. The chemical structure of this organic-inorganic material has been confirmed using ATR-FTIR. Ether segments from the 165-atom PPO-PEO-PPO backbone, and Si–O–Si networks dominate the spectra shown in Fig. 1(b). In the FTIR spectrum of a $PED_{80}S_{20}$-3 h material, the signature bands are the ether C–O–C stretching band at 1105 cm^{-1} and the CH_2 scissoring and stretching bands at 1465 and 2868 cm^{-1}, respectively [35]. Other peaks in the fingerprint region at 1248, 1283, 1345 cm^{-1} correspond to the CH_2-CH_2 anti-symmetric twisting, CH_2-CH_2 quasi-symmetric twisting, and CH_2-CH_2 asymmetric wagging, respectively [36]. The peak at 848 cm^{-1} corresponds to a coupled quasi-anti-symmetric CH_2 rocking and quasi-symmetric C-O stretching mode, while the peak at 945 cm^{-1}

correlates to a C-C stretching. Additionally, the non-stoichiometric ratio of polyether diamine and alkoxysilane used in this work leads to the strong peak at 1656 cm^{-1} resulting from the N-H scissoring vibration of unreacted diamines [37]. Compared to the ATR-FTIR spectrum of the neat polyether diamine (not shown here), the peak at 1100 cm^{-1} in the FTIR spectrum of $PED_{80}S_{20}$-3 h is more asymmetrical. This indicates that overlapping bands are present in the FTIR spectrum of $PED_{80}S_{20}$-3 h. The asymmetrical band at 1100 cm^{-1} can be attributed to a combination of the anti-symmetric stretching mode Si–O–Si [38] and the characteristic ether C–O–C stretching band. The presence of a Si–O–Si network is evidenced by the presence of the shoulder peak at 1258 cm^{-1} that correlates to the asymmetric stretching vibrations of the Si–O–Si bridging sequence [38]. The peak at 1038 cm^{-1} corresponds to the propyl chain attached to the silicon [38]. Weak shoulder peaks at 1088 cm^{-1} and the peak at 886 cm^{-1} relates to stretching vibrations of Si-OCH$_3$ and the stretching mode of Si-OH [38], indicating that hydrolysis is nearly complete. The solid-state ^{29}Si NMR analysis that will be discussed later confirms this observation. The absence of a strong, obvious peak at 910 cm^{-1} indicates that all epoxy rings are opened up and partake in the cross-linking process between polyether diamines and alkoxysilanes [38].

In the FTIR spectra of $PED_{80}S_{20}$ nanohybrid membranes that were synthesized with 1 h of condensation and modified with different ozone pre-treatment times, the peak at 1708 cm^{-1} correlates to the O-C = O ester stretch of PEGMA [39]. The intensity of this peak increases when ozone pre-treatment time
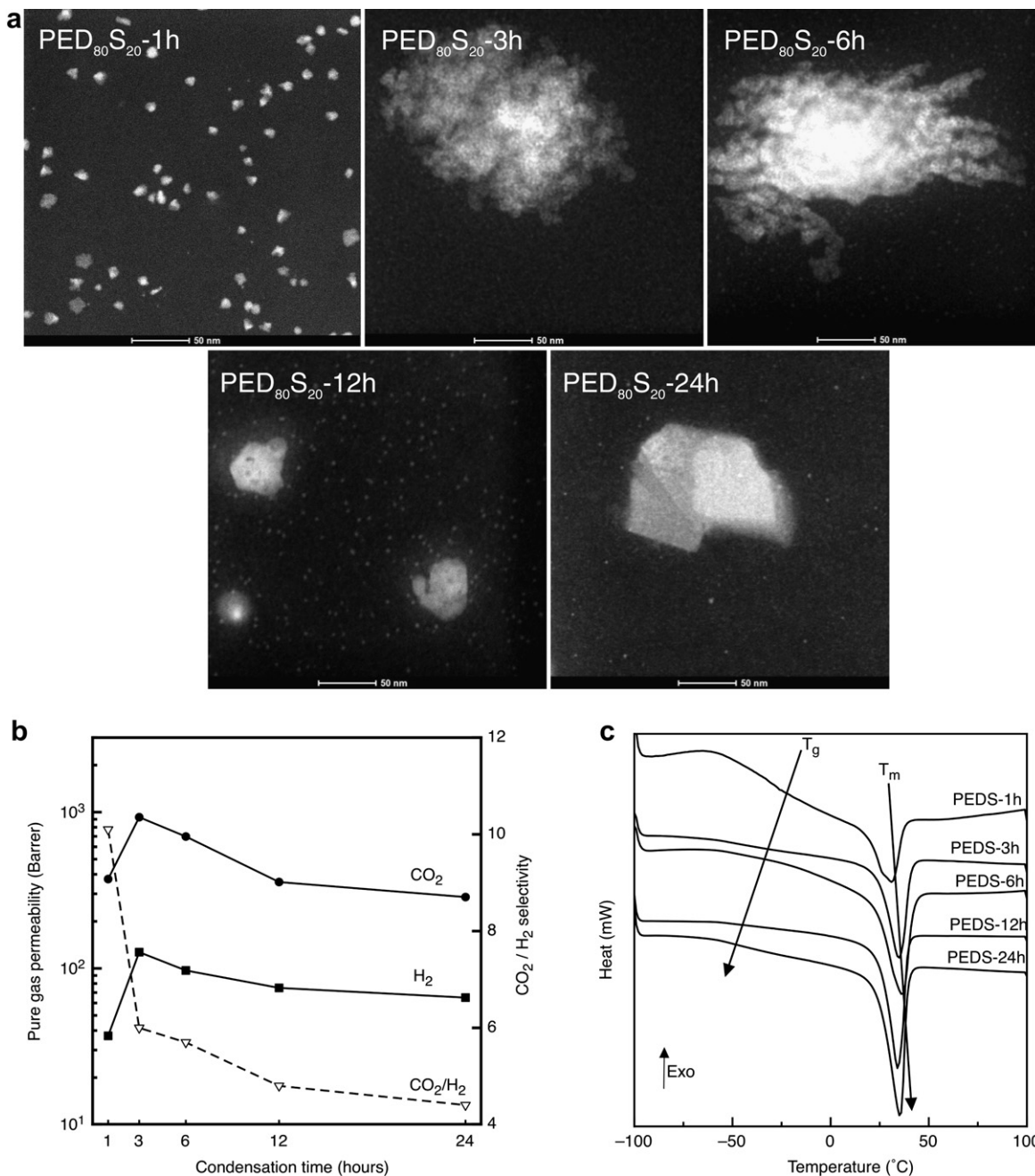
Fig. 3. (a): STEM images of $PED_{80}S_{20}$ materials synthesized using condensation durations ranging from 1 to 24 h with no ozone modification. The sizes of the silicon-based structures grow from 15 nm (1 h) to a network of 220 nm (3 h) to 500 nm (6 h). Subsequently, after 12 h of condensation, silicon-based structure sizes decrease to 60 nm. Meanwhile, there are 5 nm silicon-based nanostructures surrounding the 60 nm nanostructure. After 24 h of condensation, the silicon-based nanostructure size doubles to 150 nm (b): Pure gas permeability of $PED_{80}S_{20}$ materials synthesized with 1–24 h of condensation and no ozone pre-treatment modification. The solid squares and circles represent CO_2 and H_2 permeability, respectively. The empty inverted triangles represent the CO_2/H_2 gas selectivity of these materials. The lines provide a guide to the eye. Uncertainty in permeability measurements is ±10%. (c): DSC plot of the 2nd heating curve of $PED_{80}S_{20}$ materials synthesized using 1–24 h of condensation times. T_g and T_m values were analyzed using the STAR^e Excellence software.

increase from 30 s to 300 s, indicating that more PEGMA is grafted onto the PEDS main chains. The intensity and shape of the N-H peaks at ∼1646 and 1633 cm^{-1} remain intact. The absence of peaks ranging from 1658 to 1648 cm^{-1} indicate the absence of C=C bonds in these ozone-modified $PED_{80}S_{20}$ nanohybrid membranes i.e. PEGMA is successfully grafted onto the PEDS main chains. Additionally, the occurrence of two new peaks at 2917 and 2851 cm^{-1} correspond to the asymmetrical and symmetrical stretching modes of a methyl (CH_3) group [37]. These peaks are

more obvious in PEGMA grafted PEDS materials that contain higher contents of CH_3.

In Fig. 1(c), the presence of only T^2 (−59 ppm) and T^3 (−67 ppm) peaks in the ^{29}Si solid-state NMR of $PED_{80}S_{20}$ synthesized from different condensation and ozone pre-treatment durations indicate Si atoms that are fully condensed with siloxane bonds as well as some partially condensed Si atoms with one ethoxy or methoxy bonds and two siloxane bonds. This validates the ATR-FTIR analysis on the hydrolysis state of the alkoxysilanes.

3.2. Effects of different organic/inorganic ratio on gas transport properties of organic-inorganic membranes

EDX analyses in Fig. 2(a) indicate that the bright structures in the STEM images of the base organic-inorganic materials synthesized using different organic/inorganic ratios with 1 h of condensation, shown in Fig. 2(b) consist mainly of silicon and oxygen. Fig. 2(b) shows that as the polyether content increases from 50 wt.% to 80 wt.%, the size of the silicon-based nanostructure increases from ~5 nm to ~15 nm. The growth mechanism of the inorganic phase in materials with excess polyether content is dominated by a reaction-limited cluster–cluster aggregation [25,30]. Thus, high polyether content increases the size of the silicon-based nanostructures. In Fig. 2(c), and (d), the CO_2 and H_2 permeability, and the S_{CO_2} and D_{CO_2} coefficients of the base organic-inorganic materials increase somewhat with higher polyether content. The CO_2 affinity of the organic-inorganic material is enhanced with higher polyether content as well [27]. The similarities between the S_{CO_2} coefficients of these organic-inorganic membranes and PDMS [25,33] indicate that the silicon-based nanostructure also contribute to the high CO_2 affinity in the organic-inorganic materials. However, if the size of the silicon-based nanostructure becomes too large, CO_2 permeability will be reduced. Hence, it is important to obtain the optimal silicon-based nanostructure size. Larger CO_2 diffusion coefficients are attributed to higher relative FFV content that is a consequence of higher polyether content and larger silicon-based nanostructures. The extra methyl group in PPO increases the relative fractional free volume (FFV) content of resultant membranes [28], while the growth mechanism of the inorganic silicon-based nanostructure, steric and kinetic constraints circumvent the interpenetration and condensation of inorganic silicon-based nanostructure, leaving spaces in between the clusters of silicon-based nanostructures [30]. The increments in both S_{CO_2} and D_{CO_2} enhance the CO_2 permeability. H_2 permeability enhancements are solely attributed to the increase in relative FFV content.

3.3. Effects of condensation duration on gas permeation properties of organic-inorganic membranes

Fig. 3(a) compares the effects of the condensation duration from 1 h to 24 h on the morphology of the inorganic networks of $PED_{80}S_{20}$ materials. During the first 1–6 h of condensation, loose clusters of silicon-based nanostructures grow from 15 nm to 500 nm. The solid looking 15 nm silicon-based nanostructures agglomerate to form 500 nm irregular-shaped silicon-based nanostructures. The larger nanostructures consist of random agglomerations of the 15 nm nanostructures. As condensation duration increases to 12 and 24 h, the 500 nm irregular-shaped silicon-based nanostructures evidently transform into small, compact (~60 nm) polyhedral silicon-based nanostructures surrounded by small silicon-based nanostructures (5–15 nm). At lower magnifications, silicon-based structures with sizes up to 1–2 μm can be observed in $PED_{80}S_{20}$-24 h samples (refer to STEM image in Fig. 2(a)).

Fig. 3(b) shows that CO_2 and H_2 permeability increase as the condensation time is increased from 1 to 3 h; however, after this maximum, there is a steady decline out to 24 h of condensation. The highest CO_2 and H_2 permeability values are achieved at 3 h of condensation, while the highest CO_2/H_2 selectivity is obtained at 1 h of condensation; selectivity steadily declines with condensation time out to 24 h. As FTIR and NMR analyses have indicated that there are no chemical structure changes in these materials, the only variable among these organic-inorganic materials is the morphology and distribution of the silicon-based nanostructures. The inorganic phase morphology in $PED_{80}S_{20}$-3 h consists of loosely clustered silicon-based nanostructures (size ~ 300 nm) surrounded by

smaller silicon-based nanostructures (size ~ 5 nm). High concentrations of these small nanostructures appear to be essential for high CO_2 permeability. The materials formed using longer periods of condensation have fewer of these small nanostructures and lower CO_2 permeability. It appears that the larger silicon-based nanostructures also affect CO_2 permeability. Loose clusters of silicon-based nanostructures in $PED_{80}S_{20}$-3 h materials yield the highest CO_2 permeability while polyhedral silicon-based nanostructures that appear to possess some sort of crystallinity lead to lower CO_2 permeability. EDX analyses in Fig. 2(a) indicate that the vicinity of silicon-based microstructures contain negligible amounts of Si in the polyether matrix. This correlates to a lack of silicon-based nanostructures that can disrupt polyether chain packing that consequently leads to higher polyether crystallinity that are observed in Table 1. Hence, the lowest gas permeability is seen for the $PED_{80}S_{20}$-24 h material. Meanwhile, the inorganic phase in the $PED_{80}S_{20}$-1 h material only consists of well-distributed small clusters of silicon-based nanostructures (~15 nm). Hence, a fine balance in size heterogeneity in silicon-based nanostructures is important in enhancing CO_2 permeability while achieving good CO_2/H_2 selectivity in these organic-inorganic materials that are effectively amorphous at 35 °C. Permeation activation energies, E_p, were calculated using the Arrhenius equation $P = P_0 e^{-Ep/RT}$, where P_0 is a pre-exponential factor gas [20,40], from gas permeability data obtained over the limited temperature range of 30 °C to 45 °C. The apparent activation energy, E_p, is the sum of the activation energy required for diffusion and the heat of sorption. The E_p values in these organic-inorganic materials are 31–62 kJ/mol for H_2 and 41–51 kJ/mol for CO_2, which are smaller than those of semi-crystalline PEO [41].

PEO crystallinity can affect gas transport and separation performance [42,43]; however owing to the low melting temperature of these PEO-based materials (see Table 1) relative to the measurement temperatures used here, crystallinity plays no significant role in the results shown here. As seen in Fig. 3(c), the condensation duration also influences the glass transition (T_g) and melting temperatures (T_m) of these materials as well as the inorganic phase morphology. When condensation time increases from 1 to 12 h, T_g decreases from − 47 °C to − 60 °C. In these materials, polyether chain mobility is enhanced by the well-distributed small silicon-based nanostructures that reduce chain packing organization [44]. As most silicon-based nanostructures agglomerate to form microstructures after 24 h of condensation, the lack of well-dispersed small silicon-based nanostructures facilitates hydrogen bonding between the organic phases and slightly increases T_g to − 55 °C. The well-dispersed small silicon-based nanostructures in $PED_{80}S_{20}$-1 h, $PED_{80}S_{20}$-3 h, and $PED_{80}S_{20}$-12 h materials act as obstacles that disrupt polyether chain organization, thus the low $T_m s$. In $PED_{80}S_{20}$-24 h materials, the inorganic phase consists of

Table 1

T_g, T_m, crystallinity values (%) of working materials studied in this work. Crystallinity values were calculated with the STAR^e Excellence software and using an equation Crystallinity(%) = $\Delta H_f / (\chi_P \times \Delta H_f^0) \times 100\%$, whereby ΔH_f is the apparent heat of fusion per gram of the materials, ΔH_f^0 is the thermodynamic heat of fusion per gram of perfect PEO crystal with the value of 188.9 J/g [15] and $\Delta\chi_P$ is the weight percentage of PEO in the $PED_{80}S_{20}$ membranes.

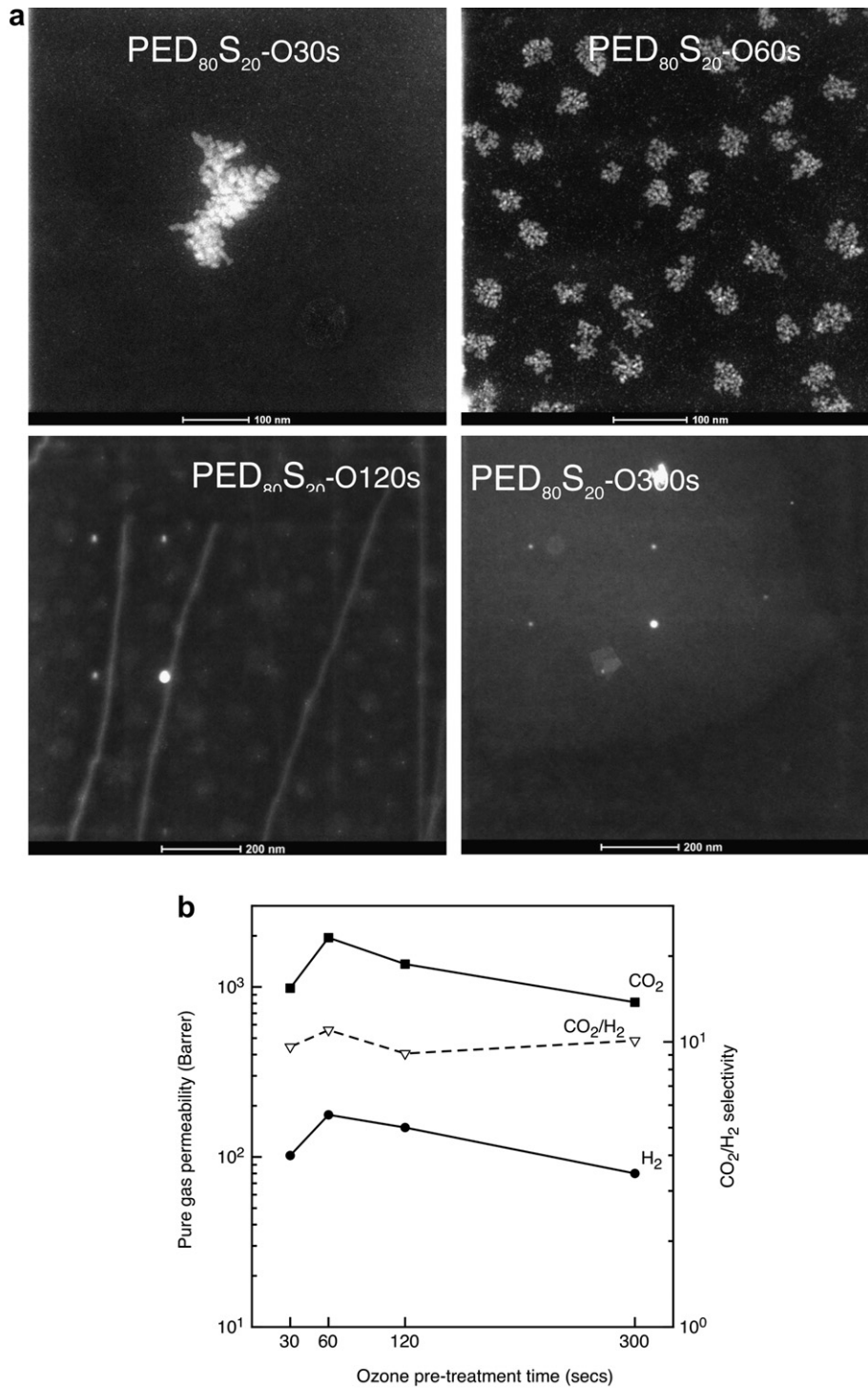| Sample code	T_g (°C)	T_m (°C)	Crystallinity (%)	P_{CO_2} (Barrer)	P_{H_2} (Barrer)	α_{CO_2/H_2}
$PED_{80}S_{20}$-1 h	−47 °C	30 °C	26%	373	36	10.1
$PED_{80}S_{20}$-3 h	−52 °C	34 °C	29%	928	154	6.0
$PED_{80}S_{20}$-6 h	−56 °C	35 °C	30%	698	127	5.7
$PED_{80}S_{20}$-12 h	−60 °C	37 °C	32%	357	75	4.8
$PED_{80}S_{20}$-24 h	−55 °C	37 °C	34%	286	65	4.4
$PED_{80}S_{20}$-o30 s	−65 °C	28 °C	25%	984	102	9.6
$PED_{80}S_{20}$-o60 s	−65 °C	24 °C	27%	1950	185	11
$PED_{80}S_{20}$-o120 s	−63 °C	25 °C	31%	1363	149	9.1
$PED_{80}S_{20}$-o300 s	−61 °C	26 °C	32%	813	80	10.1

Fig. 4. (a): STEM images of PED$_{80}$S$_{20}$ materials synthesized with 1 h of condensation; then ozone pre-treatments for 30–300 s, followed by reaction with 43 wt.% of PEGMA. As ozone pre-treatment durations increase, the silicon-based nanostructure morphology transforms from a nanocluster that resembles like a flower (after 30 and 60 s of ozone pre-treatment) to regularly spaced nanodots (after 120 s) and to high intensity nanodots in the background of a large low intensity silicon-based patch. (b): Pure gas permeability of PED$_{80}$S$_{20}$ materials synthesized with 1 h of condensation; then ozone pre-treatments for 30–300 s, followed by reaction with 43 wt.% of PEGMA. The solid squares and circles represent CO_2 and H_2 permeability, respectively. The empty inverted triangles represent the CO_2/H_2 gas selectivity of these materials. The lines provide a guide to the eye. Uncertainty in permeability measurements is ±10%.

large silicon-based microstructures that only promote localized chain packing disruptions. Overall, organization in the latter materials is more efficient, thus the higher organic phase crystallinity. High organic phase crystallinity increases the diffusion path tortuosity for gas molecules and will reduce gas permeability at temperatures below T_m.

3.4. Effect of ozone pre-treatment duration on gas transport properties of organic-inorganic materials

Modifications of the PEDS base materials via ozone pre-treatment and subsequent grafting of short alkyl chains significantly enhance gas permeability. The purpose of the ozone pre-
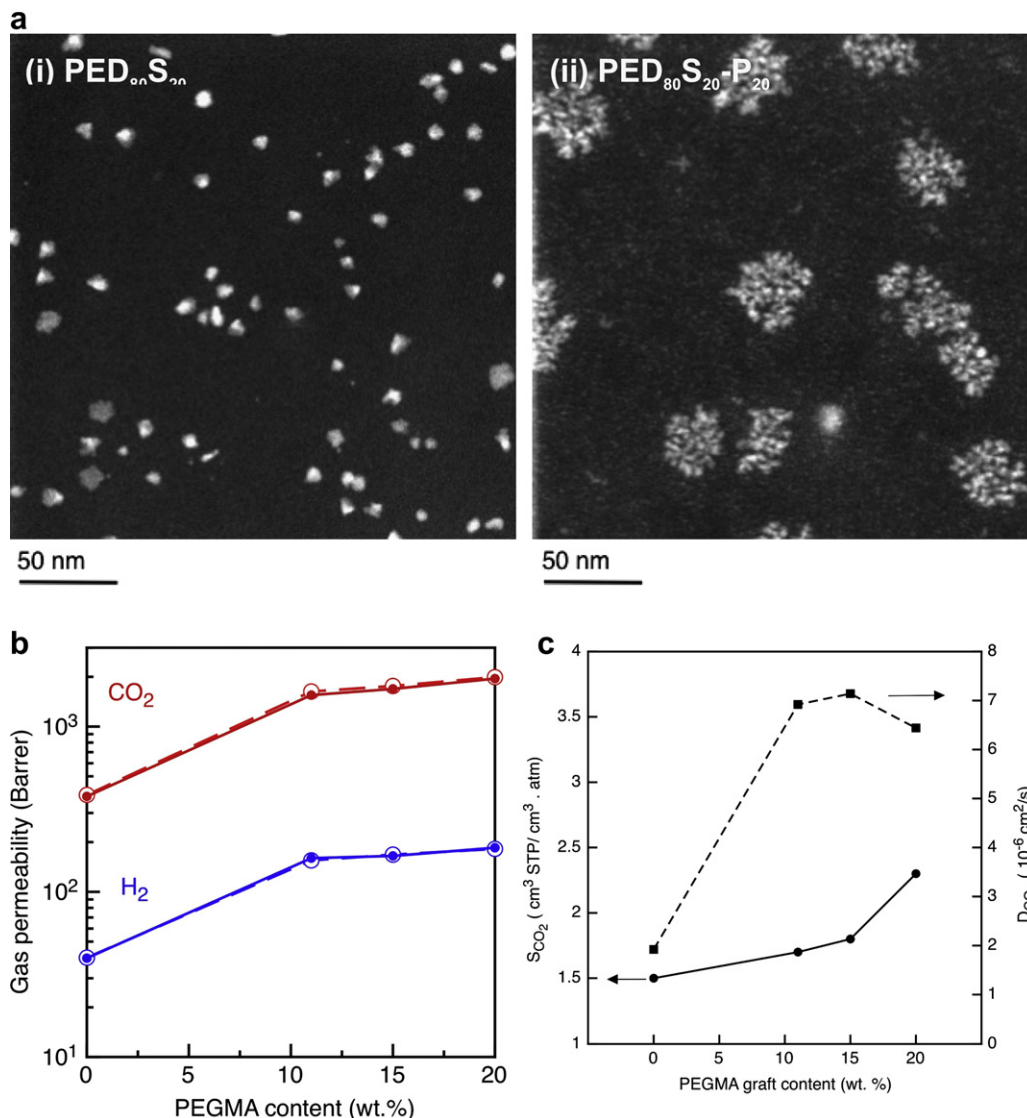
Fig. 5. (a): STEM images of (i) PED$_{80}$S$_{20}$ base material synthesized with 1 h of condensation and no ozone pre-treatment and (ii) PED$_{80}$S$_{20}$-P$_{20}$ that is synthesized with 1 h of condensation, 60 s of ozone pre-treatment, and 20 wt.% of PEGMA graft content. The nanoclusters are essential for enhancing CO$_2$ permeability. (b): Pure (solid circles) and mixed gas (empty circles) permeability of PED$_{80}$S$_{20}$ materials synthesized with 1 h of condensation and 60 s of ozone pre-treatment with different concentrations of PEGMA graft content. Mixed gas tests using 50–50 mol % CO$_2$ and H$_2$ are conducted at 35 °C while maintaining a CO$_2$ partial pressure of 3.5 atm. The mixed gas permeability is similar to the pure gas permeability, indicating that these materials can maintain high gas separation performances in situations similar to commercial settings. (c): S_{CO_2} and D_{CO_2} coefficients of PEDS materials with PED$_{80}$S$_{20}$ materials synthesized with 1 h of condensation and 60 s of ozone pre-treatment with different concentrations of PEGMA graft content. The increments in S_{CO_2} and D_{CO_2} coefficients contribute to the CO$_2$ permeability increases that far exceed the increase in H$_2$ permeability, hence the high CO$_2$/H$_2$ selectivity. The solubility coefficients of PEGMA grafted PEDS nanohybrid materials resemble those of silicon-based polymers like PDMS (1.3 cm^3 STP/cm^3. atm) [41].

treatment is to introduce peroxide moieties onto the main PED$_{80}$S$_{20}$ main chains, so that subsequent thermal decomposition of these peroxide functional groups can facilitate PEGMA grafting. The degree of modification can be controlled over the ozone pre-treatment duration. The concentration of graft initiation sites, i.e., peroxide moieties on the base PEDS material, decreases with shorter ozone pre-treatment durations [45]. Fewer graft initiation sites reduce the PEGMA graft content, i.e., the amount of unreacted PEGMA in the synthesis solution will increase. The −OH moieties in these unreacted PEGMA can easily hydrogen bond with water molecules, thus reducing the interaction between water and silicon i.e., reducing the water/silicon ratio [33], thus resulting in agglomerations of silicon-based nanostructures that are observed in Fig. 4(a). With lesser graft initiation sites, the only way to increase PEGMA graft content is via a chain propagation mechanism that should yield longer PEGMA chains [25]. Increasing the

ozone pre-treatment duration leads to smooth-looking, and compact silicon-based nanostructures that seem to be regularly spaced apart. Higher PEGMA graft content with longer pre-ozone treatment time [45] reduces the amount of unreacted PEGMA in the synthesis solution, i.e., more water molecules are engaged by the sol-gel reaction during the synthesis procedure [25,30,33]. This maintains a high water/silicon ratio that favors a hydrolytic depolymerization, whereby the "nucleation and growth" mechanism is dominant and yields small compact silicon-based nanostructures [30]. Because of the morphological changes in the inorganic phase, the CO$_2$ permeability of ozone-modified membranes increases with longer ozone pre-treatment durations in Fig. 4(b). The ideal ozone pre-treatment duration is 60 s whereby 15 nm silicon-based nanostructures randomly agglomerate into flower-like 50 nm silicon-based nanoclusters. Such silicon-based nanoclusters seem to surround some organic material and are required for enhancing
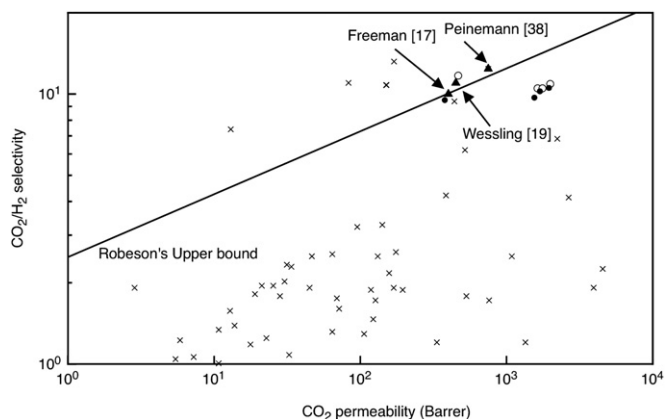
Fig. 6. A comparison of the CO_2/H_2 separation performance of our nanohybrid membranes with Robeson's upper bound [37] and other membrane materials described in recent literature [17,38–40]. Although the performance of these nanohybrid membranes lies below the upper bound line, the tremendous improvement in CO_2 permeability whilst maintaining high CO_2/H_2 selectivity renders these materials attractive for industrial applications.

CO_2 permeability. The increment in H_2 permeability is larger in proportion to the enhancements in CO_2 permeability; thus, the lower CO_2/H_2 selectivity that is observed in materials that have undergone prolonged periods of ozone pre-treatments.

3.5. Effect of side chain concentration on gas transport properties of organic-inorganic materials

The $PED_{80}S_{20}$ materials synthesized by 1 h of condensation and 60 s of ozone pre-treatment were modified by controlling the PEGMA graft content on the PEDS main chains. The PEGMA graft content is determined by comparing the weight of the membranes before and after washing. Results indicate that 11, 15, and 20 wt.% of PEGMA is grafted onto the base materials when 27, 33 and 43 wt.% of PEGMA was initially added to the $PED_{80}S_{20}$ solution. The incorporation of PEGMA enhances polar ether oxygen content that augments S_{CO_2} and increases the relative FFV content of the membrane [25]. In Fig. 5(a), the size of the silicon-based nanostructures increases with higher PEGMA graft content. Compared to the silicon-based nanostructures in the $PED_{80}S_{20}$ base material, the silicon-based nanostructures in $PED_{80}S_{20}$ materials grafted with PEGMA are much larger; hence displaying the effects of PEGMA presence on silicon-based nanostructures. With larger silicon-based nanostructures, Fig. 5(b) shows that PEGMA grafts significantly enhance gas permeability while maintaining high CO_2/light gas selectivity. The highest CO_2 permeability is achieved when 20 wt.% of PEGMA is grafted onto the PEDS base material. The significant enhancements in CO_2 permeability is due to increases in both S_{CO_2} and D_{CO_2} as a function of PEGMA graft content in Fig. 5(c). The ideal synthesis protocol for high CO_2 permeability and good CO_2/H_2 selectivity appears to be the combination of 1 h of condensation, 60 s of ozone pre-treatment and 20 wt.% of PEGMA grafted onto a base $PED_{80}S_{20}$ material. The CO_2 transport properties of the optimized nanohybrid membrane (shown in Fig. 6) exceed those of other rubbery CO_2-philic membranes [20,26,46–49], while maintaining similar CO_2/H_2 selectivity. The significantly enhanced CO_2 transport properties of these nanohybrid materials have overcome the inadequacy of current PEO-based membranes for industrial applications.

4. Conclusion

The CO_2 permeability of this ideal nanohybrid membrane is in the same range of CO_2 permeability as PDMS [50], thus it is comparable to PDMS, albeit with a higher CO_2/H_2 selectivity. The effects of condensation and modification durations greatly impact the silicon-based nanostructures morphology and distribution that consequently play important roles in determining CO_2 permeability. Silicon-based structure size heterogeneity in these nanohybrid membranes appears to be the key to high CO_2 permeability and good CO_2/H_2 selectivity. Ideally, silicon-based nanostructures with sizes up to 50 nm surrounded by 5–15 nm silicon-based nanostructures is the preferred inorganic phase morphology that yields optimal nanohybrid membranes. As this work illustrates the relationship between synthesis and modification conditions, and gas permeability, tailored nanohybrid membranes can be easily fabricated according to requirements. Moreover, this work has also provided an insight on inorganic phase morphological changes in sol-derived materials that are commonly used in many other applications. Till date, wet spinning of PEO-based hollow fibers remains elusive. However, this problem can be overcome by coating this PEO-based nanohybrid materials onto a hollow fiber substrate. Such an approach is highly advantageous for amorphous PEO-based materials that possess non-ideal mechanical properties. Moreover, a previous work by Shao and Chung [20] has shown that silica nanoparticles enhanced the mechanical properties of similar low-crystallinity PEO-based nanohybrid materials. Future works will be explored on how to design composite hollow fibers by applying this newly developed material on microporous substrates for gas separation as demonstrated elsewhere [51].

References

[1] Williams LO. Hydrogen, the optimum fuel. An end to Global Warming. Oxford: Pergamon; 2002. pp. 89–102.
[2] Service RF. Science 2004;305(5686):958–61.
[3] Song C. Catalysis Today 2006;115(1–4):2–32.
[4] Shao L, Low BT, Chung T-S, Greenberg AR. Journal of Membrane Science 2009; 327(1–2):18–31.
[5] Jones CA, Gordeyev SA, Shilton SJ. Polymer 2011;52(4):901–3.
[6] Murphy TM, Langhe DS, Ponting M, Baer E, Freeman BD, Paul DR. Polymer 2011;52(26):6117–25.
[7] Horn NR, Paul DR. Polymer 2011;52(24):5587–94.
[8] Cui L, Qiu W, Paul DR, Koros WJ. Polymer 2011;52(24):5528–37.
[9] Chao W-C, Huang S-H, An Q, Liaw D-J, Huang Y-C, Lee K-R, et al. Polymer 2011;52(11):2414–21.
[10] Sakaguchi T, Tominaga S, Hashimoto T. Polymer 2011;52(10):2163–9.
[11] Yilgor E, Eynur T, Kosak C, Bilgin S, Yilgor I, Malay O, et al. Polymer 2011; 52(19):4189–98.
[12] . Pomogailo AD. Russian Chemical Reviews 2000;69(1):53–80.
[13] Hajji P, David L, Gerard JF, Pascault JP, Vigier G. Journal of Polymer Science Part B: Polymer Physics 1999;37(22):3172–87.
[14] Kanezashi M, Sano M, Yoshioka T, Tsuru T. Chemical Communications 2010; 46(33):6171–3.
[15] Süer MG, Baç N, Yilmaz L. Journal of Membrane Science 1994;91(1–2):77–86.
[16] Chung T-S, Jiang LY, Li Y, Kulprathipanja S. Progress in Polymer Science 2007; 32(4):483–507.
[17] Vu DQ, Koros WJ, Miller SJ. Journal of Membrane Science 2003;211(2):311–34.
[18] Hill RJ. Physical Review Letters 2006;96(21):216001.

[19] Patel NP, Zielinski JM, Samseth J, Spontak RJ. Macromolecular Chemistry and Physics 2004;205(18):2409–19.
[20] Shao L, Chung T- S. International Journal of Hydrogen Energy 2009;34(15):6492–504.
[21] Voorhees PW. Journal of Statistical Physics 1985;38(1):231–52. 252.
[22] Sforça ML, Yoshida IVP, Nunes SP. Journal of Membrane Science 1999;159(1–2):197–207.
[23] Lim C, Hong S-I, Kim H. Journal of Sol-Gel Science and Technology 2007;43(1):35–40.
[24] Cao G, Lu Y, Delattre L, Brinker CJ, López GP. Advanced Materials 1996;8(7):588–91.
[25] Lau CH, Liu S, Paul DR, Xia J, Jean Y-C, Chen H, et al. Advanced Energy Materials 2011;1(4):634–42.
[26] Lin H, Van Wagner E, Freeman BD, Toy LG, Gupta RP. Science 2006;311(5761):639–42.
[27] Lin H, Freeman BD. Marcomolecules 2006;39:3568–80.
[28] Raharjo RD, Lin H, Sanders DF, Freeman BD, Kalakkunnath S, Kalika DS. Journal of Membrane Science 2006;283(1–2):253–65.
[29] Wen J, Wilkes GL. Chemistry of Materials 1996;8(8):1667–81.
[30] Brinker CJ. Journal of Non-Crystalline Solids 1988;100(1–3):31–50.
[31] Czichos H, Saito T, Smith L. Springer handbook of materials measurement methods. Springer; 2006.
[32] Wang R, Cao C, Chung T-S. Journal of Membrane Science 2002;198(2):259–71.
[33] Lau CH, Chung TS. Macromolecules 2011;44(15):6057–66.
[34] Stern SA. Journal of Polymer Science Part A-2: Polymer Physics 1968;6(11):1933–4.
[35] Schmidt P, Dybal J, Sturcov· A. Vibrational Spectroscopy 2009;50(2):218–25.
[36] Brian CS. Fundamentals of fourier transform infrared spectroscopy. Boca Raton: CRC Press; 1996.
[37] Silverstein RM, Webster FX, Kiemle DJ. Spectrometric identification of organic compounds. 7th ed. New Jersey: John Wiley & Sons; 2005.
[38] Heitz C, Laurent G, Briard R, Barthel E. Journal of Colloid and Interface Science 2006;298(1):192–201.
[39] Chen J, Nho Y, Kwon O, Hoffman A. Journal of Radioanalytical and Nuclear Chemistry 1999;240(3):943–8. 948.
[40] Yampolskii Y, Shishatskii S, Alentiev A, Loza K. Journal of Membrane Science 1998;148(1):59–69.
[41] Lin H, Freeman BD. Journal of Membrane Science 2004;239(1):105–17.
[42] Bondar VI, Freeman BD, Pinnau I. Journal of Polymer Science Part B: Polymer Physics 1999;37(17):2463–75.
[43] Horas JA, Rizzotto MG. Polymer Engineering & Science 1999;39(8):1389–93.
[44] Chen H-W, Jiang C-H, Wu H-D, Chang F-C. Journal of Applied Polymer Science 2004;91(2):1207–16.
[45] Chen Y, Ying L, Yu W, Kang ET, Neoh KG. Macromolecules 2003;36(25):9451–7.
[46] Robeson LM. Journal of Membrane Science 2008;320(1–2):390–400.
[47] Yave W, Car A, Funari SS, Nunes SP, Peinemann K-V. Macromolecules 2009;43(1):326–33.
[48] Reijerkerk SR, Arun A, Gaymans RJ, Nijmeijer K, Wessling M. Journal of Membrane Science 2010;359(1–2):54–63.
[49] Xia J, Liu S, Lau CH, Chung T-S. Macromolecules 2011;44(13):5268–80.
[50] Merkel TC, Bondar VI, Nagai K, Freeman BD, Pinnau I. Journal of Polymer Science Part B: Polymer Physics 2000;38(3):415–34.
[51] Chen HZ, Xiao YC, Chung T-S. Journal of Membrane Science 2011;381(1–2):211–20.